Geomech. Geophys. Geo-energ. Geo-resour. (2025) 11:4
https://doi.org/10.1007/s40948-024-00921-3

RESEARCH

Generating H_2 during the CO_2 sequestration in basalt formations

Lizhi Huang · Quansheng Liu · Carl Steefel · Yiwei Liu · Mengsu Hu · Shimin Liu · Yiheng Zhang · Xuhai Tang

Received: 12 September 2024 / Accepted: 23 December 2024 / Published online: 11 January 2025
© The Author(s) 2025, corrected publication 2025

Abstract This work demonstrates the potential of generating H_2 and geologically storing CO_2 simultaneously in basalt formations. Basalt is able to produce H_2 in CO_2-saturated water at a rate of 46.68 ppm d^{-1} under 25 °C, with generation rates leveling off after 6 days. At the reaction temperature of 60 °C, the cumulative hydrogen production of basalt for 5 days reaches 11,960 ppm, and its daily hydrogen production rate is more than 51 times that of 25 °C. The CO_2-acidified experiment produced the most H_2, presumably due to the pH buffering of the CO_2 system. The water–solid reaction interface provided by basalt is essential for H_2 production. Scanning electron microscopy (SEM) results show that substantial nano-sized mineral precipitate formed on the basalt surfaces. Electronic microprobe results (EMPA) show that carbonate minerals are formed after the reaction of basalt with CO_2 and water under ambient temperature conditions. Thermogravimetric analysis (TG) results show a mineral carbonation efficiency of 4.17% in 3 months. The present experimental results demonstrate the technological feasibility of producing hydrogen for the energy transition while storing CO_2 geologically, thus mitigating anthropogenic emissions of a greenhouse gas and also creating revenue for CCS.

Article highlights

1. This work demonstrates the feasibility of simultaneously generating H_2 while storing CO_2 geologically in basalt formations.
2. CO_2 induced the release Fe(II) from basalt, which enhances the production of H_2.
3. Substantial enhancement of H_2 production was observed with increased temperature.

Keywords CO_2 mineralization · Basalt · Hydrogen generation · CCS

L. Huang · Q. Liu · Y. Liu (✉) · Y. Zhang · X. Tang (✉)
School of Civil Engineering, Wuhan University, Wuhan 430072, China
e-mail: liuyiwei@whu.edu.cn

X. Tang
e-mail: xuhaitang@whu.edu.cn

C. Steefel · M. Hu
Lawrence Berkeley National Laboratory, Berkeley, CA, USA

S. Liu
Department of Energy and Mineral Engineering, G3 Center and EMS Energy Institute, The Pennsylvania State University, University Park, State College, PA 16802, USA

1 Introduction

In the context of global warming and climate change, the development and implementation of Carbon Capture and Storage (CCS) technologies appear as

an unavoidable mid-term solution (Bui et al. 2018). In particular, the sequestration of CO_2 in solid form through carbon mineralization combines the advantages of deep geological storage with increased safety compared with classical deep saline aquifer storage (Kainiemi et al. 2015). Hydrogen gas (H_2) has long been recognized as an energy vector (Momirlan and Veziroglu 2002). Recent awareness of reducing the world's carbon dependency has boosted the need for novel energy solutions, such as promoting hydrogen, partly because of its sole by-product of combustion, water (Evro et al. 2024). Indeed, H_2 is able to be oxidized without releasing any CO_2 and transformed into electricity through fuel cells, and stored in large quantities as any gaseous component (Yue et al. 2021). However, CCS and H_2 production have to face different challenges. This work aims to combine the CCS and H_2 production while addressing their individual challenges.

Despite the importance of CCS for achieving clean energy transitions, CCS strategies have been slow to be deployed (Durmaz 2018). There are two main barriers: 1) CCS is expensive. Carbon policies are not strong enough and carbon pricing is not high enough to make CCS economically attractive; 2) the stability and security of the long-term storage of CO_2 are unclear (Rutqvist 2012; Fender et al. 2020; Longden et al. 2022; Mahjour and Faroughi 2023). The high cost associated with realizing carbon capture projects at scale is a major barrier to more widespread adoption. Operating costs for CCS can be reduced through a combination of technical innovation and support from policymakers around the world, such as carbon tax schemes (Sun and Chen 2022). In-situ mineralization storage of CO_2 is one of the essential methods that has been demonstrated to date. For example, it was found that over 95% of the CO_2 injected into the reactive basalt at the CarbFix site in Iceland was rapidly mineralized to carbonate minerals in less than two years (Gislason and Oelkers 2014; Matter et al. 2016). The Wallula pilot project in the United States also confirmed rapid mineralization of CO_2 in basalt formations (McGrail et al. 2017). This process involves dissolving CO_2 in water and injecting it into basaltic rocks, where it reacts with calcium, magnesium, and iron ions from the rock to form stable carbonate minerals. The key to this rapid mineralization is the dissolution of basalt, which releases necessary ions, and the mixing of injected water with alkaline formation waters, leading to the precipitation of carbonates and effectively sequestering CO_2. This approach not only offers a permanent solution for CO_2 storage but also significantly reduces the risk of carbon leakage. However, the high cost of CCS remains a significant challenge without a viable solution.

Hydrogen is considered to be a key component of the decarbonization strategy for large parts of the transport system, as well as for some heavy industries (Kelley et al. 2005; Greening et al. 2016; Truche et al. 2020; Zgonnik 2020; Boreham et al. 2021; Milkov 2022). For a long time, there was a misconception that free hydrogen in nature is rare, and thus it has been neglected (Smith et al. 2005). Recently, scientists have confirmed that molecular hydrogen is far more widespread in nature than previously believed, with high concentrations of natural hydrogen reservoirs being discovered (Zgonnik 2020; Blay-Roger et al. 2024). Over a hundred instances of natural hydrogen concentrations exceeding 10% volume have been reported, primarily in Eastern Europe and Northern Asia (Zgonnik 2020). This prevalence is largely due to early recognition and more frequent searches for geological hydrogen by researchers in these regions. Natural hydrogen production mechanisms involve water–rock reactions such as serpentinization, radiolysis, and silicon radical-induced water reduction (Hand 2023). The mechanisms of H_2 production in aqueous systems are also well-understood, with production rates increasing with temperature and varying from silicic to mafic and ultramafic rocks. The extent of hydrogen production is influenced by factors including rock composition, temperature, water-to-rock ratio, fluid salinity, and the distribution of iron among the alteration products (McCollom and Bach 2009; Leong and Shock 2020). Hydrogen is commonly produced at high temperatures through the hydration of mafic and ultramafic rocks. McCollom and Bach (2009) explored the H_2 production during the serpentinization of ultramafic rocks (McCollom and Bach 2009). The process involves the reaction of water with iron-rich minerals (such as olivine and pyroxene) present in the rocks, where ferrous iron (Fe(II)) is oxidized to form magnetite while hydrogen from the water is reduced to H_2. Mayhew et al. (2013) investigated the process and mechanisms of hydrogen generation from low-temperature (< 100℃) water–rock reactions and concluded that the presence

of spinel phases in ultramafic and mafic rocks plays a crucial role in promoting hydrogen generation at low temperatures (Mayhew et al. 2013). However, the exact processes by which geological hydrogen forms, migrates, and potentially accumulate in commercially viable quantities remain unclear. The exploration and extraction of natural hydrogen have become a burgeoning field, with the potential to revolutionize future energy use. In fact, hydrogen wells are already being exploited commercially. While geologic hydrogen offers considerable promise, realizing its full resource potential requires further investigation to reduce the uncertainty surrounding the components of the hydrogen system and to develop exploration strategies.

Enhanced geological hydrogen production is a promising exploration strategy in which injection of water into iron-rich rocks leads to generation of hydrogen. This approach for generating hydrogen becomes even more attractive if the stimulated hydrogen production process can be coupled with in situ mineralization storage of CO_2. Although this hypothesis has been recently proposed (Hand 2023), the interaction between CO_2 sequestration and hydrogen production is rarely reported and poorly understood. Osselin et al. (2022) reported a case of the reaction of $NaHCO_3$-rich brine with natural serpentinite cores at 100–200 bar and 280 °C, which resulted in 5.6% of CO_2 sequestration (quantity of CO_2 stored over quantity injected) and 0.8% of H_2 production during the 10 to 14 days of the experiments (Osselin et al. 2022). Kularatne et al. 2018 discussed the use of olivine-bearing mine tailings reacted with CO_2-saturated water under conditions between 473 and 573 K and 15 to 30 MPa, while producing hydrogen gas (Kularatne et al. 2018). These reaction conditions are too stringent for engineering applications in both temperature and pressure. Compared with that, the reservoir conditions for CarbFix are replicable, with the temperature range from 20 to 50 °C and pressure at ~3.36 bar (Aradóttir et al. 2012). The potential for geological hydrogen production and rapid sequestration in basalt formations is promising, sparking our interest in exploring reactive basalt for hydrogen production.

In this work, we conducted the basalt-involved simultaneous H_2 generation and CO_2 mineralization experiments at 25 ℃ and 60 ℃, with daily monitoring of H_2 production. The experimental results confirm the feasibility of carbon sequestration and hydrogen production in basalt. To elucidate the underlying mechanisms, we employed X-ray photoelectron spectroscopy (XPS), Fourier Transform Infrared (FTIR) spectroscopy, scanning electron microscopy (SEM), electron probe microanalysis (EMPA), and thermogravimetric (TG) analysis on the reaction products. The analysis of the results provides a detailed understanding of the mechanisms of hydrogen production during the reaction between basalt, CO_2, and water. This study highlights a promising approach to hydrogen generation during CO_2 geological storage, which simultaneously enhances CO_2 mineralization, increases the safety of CO_2 geological storage, and creates potential new revenue streams for CCS projects.

2 Materials and experimental methods

2.1 Sample collection and preparation

Fresh basalt samples were collected from a site near Haikou, China. The basalt samples are dark gray, with fine-grained texture and unobvious vesicular structure. The surface of basalt is evenly distributed with visible pores (see Fig. 1a). Basalt samples are first cut into blocks and the mineral composition of the basalt is quantified using the TESCAN Integrated Mineral Analyzer (TIMA). It utilizes detectors such as back-scattered electron (BSE), secondary electron (SE), and energy-dispersive X-ray spectroscopy (EDS) to collect comprehensive data on mineral concentration, element distribution, and properties. TIMA operates in high-resolution mapping mode, collecting BSE signals at 1 μm pixel spacing, and identifies minerals by comparing the collected spectra with a library of standard mineral spectra. This allows for the detailed visualization and analysis of mineral geometries and distributions. The primary minerals in the sample basalt include 39.42% pyroxene, 37.65% plagioclase, 19.51% olivine, and 2.16% ilmenite, with trace amounts of other minerals (see Fig. 1b).

The basalt sample was ball-milled to basalt powder to increase the surface area of the rock sample and thus maximize reaction rates. Basalt particles were crushed in an oxygen-free ball mill to prevent

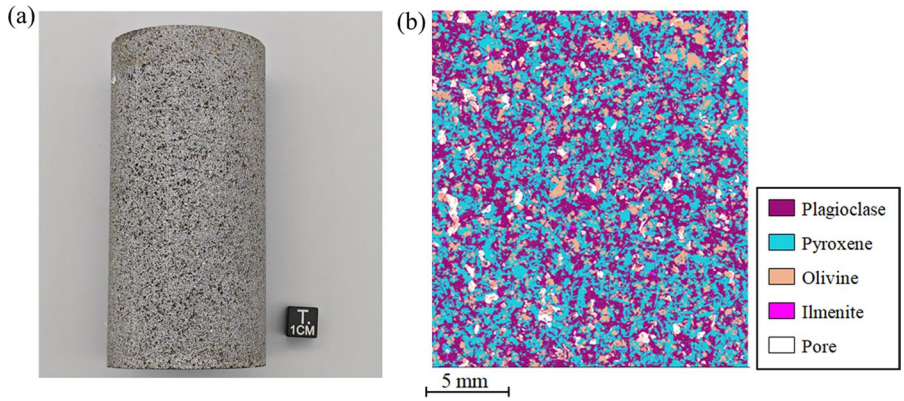


Fig. 1 Information on the basalt sample. **a** Photo of the basalt sample, **b** mineral distribution obtained by TIMA

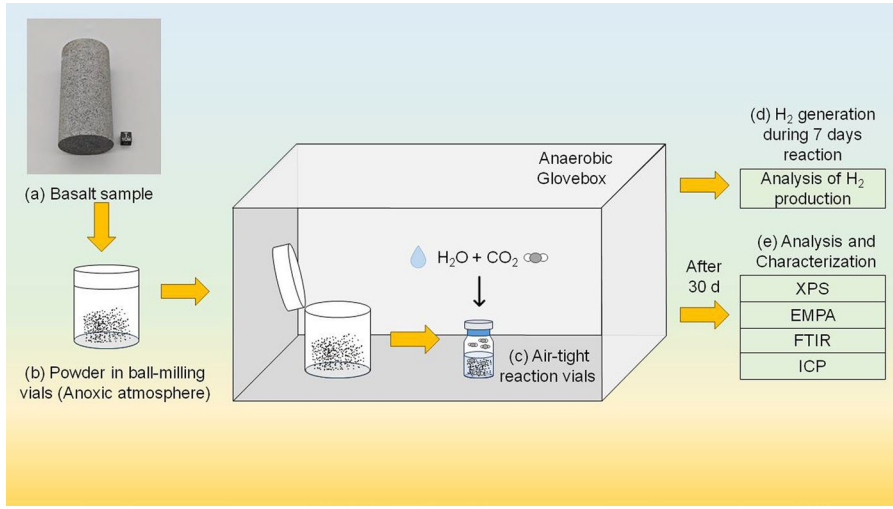


Fig. 2 Experimental setup for the water-CO_2-basalt reaction. **a** Basalt sample. **b** Ball milling in ball-milling vials under an anoxic N_2 atmosphere. **c** Carry out the basalt-CO_2-water reaction in air-tight reaction vials in anaerobic glovebox. **d** H_2 was monitored for 7 days reaction. **e** Analysis and characterization after 30 days

oxidation during grinding for small-scale experiments in small vials, which require minimal sample weight. Basalt and forty zirconia balls (0.6 cm in diameter) were all placed into ball-milling vials in the glovebox to achieve anaerobic conditions. The ball-milling vials were sealed and taken out from the glovebox, followed by the ball-milling treatment at 450 rpm for 20 h. Long-time ball-milling is used to significantly increase the surface area of basalt particles, thereby producing sufficient H_2 for detection. For larger-scale experiments requiring more basalt, a ceramic mortar and pestle were used to crush the basalt manually, and the crushed material was then sieved to obtain particles smaller than 200 mesh.

2.2 Basalt-CO_2-water reactions at 25℃

The ball-milled basalt was placed into air-tight reaction vials containing CO_2-saturated solution and CO_2 headspace. Basalt-CO_2-water reactions in the vials were conducted in the glovebox at 25 ℃ (see Fig. 2). Each vial carried 5 mL ultrapure water, 0.1 g ball-milled basalt powder, and extra CO_2 in the headspace. Reaction durations for H_2 analysis were 1 day, 2 days, 3 days, 4 days, 5 days, 6 days, and 7 days, respectively. To assess the experimental error, replicate analyses were conducted. Three tests were performed for every duration to obtain statistical results. Basalt samples reacted for 30 days were collected by centrifugation dried in the anaerobic glovebox and then subjected to solid-state characterizations.

Table 1 Experimental groups in air-tight reaction vials

Group	Reactant	Temperature (°C)	Duration (days)
A	Basalt-CO_2-water	25	1,2,3,4,5,6,7,30
B	Basalt-water-Fe^{2+}	25	1
C	Basalt-water	25	1
D	Basalt-water–HCl	25	1
E	Water-Fe^{2+}	25	1
F	Water-CO_2	25	1

The CO_2-saturated solution was prepared by bubbling solid CO_2 in pure water for at least 20 min. To dissolve the CO_2 sufficiently, the solid CO_2 is thrown into the vial and constantly shaken. Solid CO_2 dissolves in pure water during gasification while displacing air in headspace. Before the solid CO_2 was about to disappear, the vial was sealed. In this way, the CO_2-saturated aqueous solution is obtained, and the headspace is filled with CO_2 to supplement the reaction consumption in time. The pH of CO_2-saturated water at ambient pressure is approximately 5.0.

To investigate the effect of the Fe^{2+} on H_2 production, a series of experiments were conducted and compared, including the basalt-CO_2-water reaction (group A), basalt-water-Fe^{2+} reaction (group B), basalt-water reaction (group C), basalt-water–HCl reaction (group D), water-Fe^{2+} reaction (group E) and water-CO_2 reaction (group F) (as listed in Table 1). Reactants in group A are as described above. In group B, 2 mM of Fe^{2+} was introduced into the solution. In group C, only water and basalt were included. In group D, the pH of basalt suspensions was adjusted to ~5.0 using 1 M HCl, matching the pH of CO_2-saturated water. In group E, 2 mM of Fe^{2+} and water were included. In group F, only water and CO_2 were included. All the experiments were conducted in air-tight reaction vials for 1 day and repeated 3 times.

2.3 Basalt-CO_2-water reaction at 60℃

To investigate the impact of temperature, larger-scale basalt-CO_2-water reactions were performed in 1000 mL anaerobic flasks. Each anaerobic flask contains 800 g of basalt powder and 800 mL of pure water. Excess solid CO_2 was added, and the flask was then sealed. The flasks were placed in a water bath at 60 °C and room temperature (25 °C). Three sets of tests were conducted, including basalt-CO_2-water at 60 °C, basalt-CO_2-water at 25 °C, and control flasks containing only water and CO_2 at 60 °C (as listed in Table 2). Due to the difficulty in keeping the air tightness in anaerobic flasks, the reaction time for detecting hydrogen is up to 5 days. For each set, reaction durations were 1 day, 3 days, and 5 days, respectively.

Table 2 Experimental groups in 1000 mL anaerobic flasks

Group	Reactant	Temperature (°C)	Duration (days)
G	Basalt-CO_2-water	60	1,3,5
H	Basalt-CO_2-water	25	1,3,5
J	Water-CO_2	60	1,3,5

2.4 H_2 quantification

Following the treatment, the quantity of H_2 generated after different days of reaction was measured (Fig. 2d). For a specific time interval, a 1 mL headspace gas sample was withdrawn using an air-tight spring, with H_2 analysis following immediately. The H_2 was analyzed on gas chromatography (GC-7890B, Agilent) equipped with a high-sensitivity thermal conductivity detector (TCD) and a molecular sieve column (length: 30 m, inner diameter: 0.32 mm, film thickness: ¼ μm). The temperature program was set as follows: the initial oven temperature was 40 °C, held for 5 min, then increased at a rate of ¾°C/min to 80 °C, and finally held at 80 °C for 10 min. GC was calibrated using a certified standard gas mixture containing known concentrations of H_2 (0.1%, 0.5%, 1%, 2%, and 5% in N_2). The detection limit (LOD) for H_2 was determined based on the signal-to-noise ratio (S/N) of 3:1. The LOD for H_2 was found to be 0.1 ppm, which is well below the typical concentrations encountered in our experiments.

2.5 Characterization of chemical alterations

2.5.1 X-ray photoelectron spectroscopy (XPS)

The chemical composition and elemental valence of the basalt samples were characterized via XPS (ESCALAB250Xi, Thermo VG Scientific, USA). The XPS was calibrated using the C1s (284.80 eV) peak

as a reference. The samples were dried into a powder form in a glovebox, and then pressed into pellets and affixed onto sample holders with dimensions of approximately 3 × 3 mm. The prepared samples were subsequently submitted for XPS analysis.

2.5.2 Fourier transform infrared spectroscopy (FTIR)

The functional groups present in the basalt samples were characterized using FTIR, employing a Nicolet 5700 spectrometer. The basalt samples were first ground into fine powders to ensure a homogeneous distribution of the material. These powders were then mixed with potassium bromide (KBr) and pressed into thin, transparent discs to facilitate infrared light transmission. The FTIR spectra were recorded over a wavenumber range of 4000 to 400 cm^{-1}, with a resolution of 4 cm^{-1}. Background spectra of pure KBr were also collected under identical conditions to correct for any instrumental or environmental interferences. The obtained spectra were analyzed to identify and quantify the characteristic absorption bands associated with various functional groups within the basalt samples, providing insights into their chemical composition and structure.

2.5.3 Ion concentration charaterization

The changes in ion concentrations in the leachate derived from basalt were quantitatively determined using Inductively Coupled Plasma Mass Spectrometry (ICP-MS) or Inductively Coupled Plasma Optical Emission Spectrometry (ICP-OES). To prepare the samples for analysis, the leachate solutions were filtered through 0.45 μm polytetrafluoroethylene (PTFE) filters to remove any suspended particulates that could interfere with the measurements. Aliquots of the filtered leachates were then diluted with 2% nitric acid (HNO_3) to ensure proper ionization efficiency and to prevent precipitation of metal ions.

2.6 Characterization of carbon mineralization

2.6.1 Electron probe microanalysis (EPMA)

Electron probe microanalysis (EPMA) was used to confirm carbon mineralization using a JEOL JXA-8230 electron microprobe. The operating conditions were as follows: beam current was 1×10^{-8} A, accelerating voltage was 15 kV, and beam spot size was 3 μm.

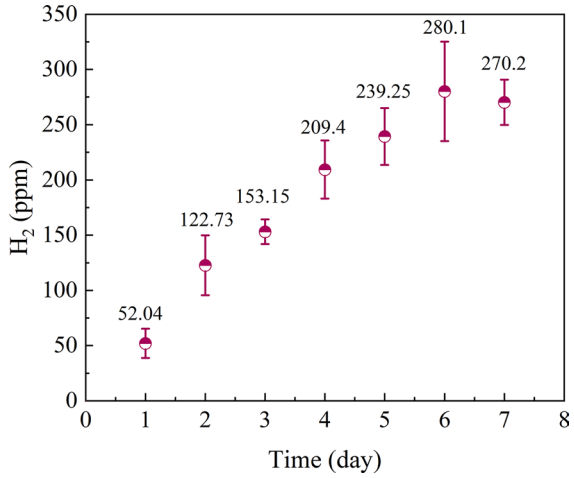


Fig. 3 H_2 production from water-CO_2-basalt rocks reactions at 25 °C. No H_2 was observed from water-CO_2 reactions without basalt rocks. The vertical bars show the results of duplicate experiments

2.6.2 SEM and thermo-gravimetric (TG) analysis

SEM and thermogravimetric analysis (TG) were then used to characterize the carbon mineralization in a bulk basalt sample before and after the reaction. To obtain high-resolution SEM images, gold powder was sprayed for 60 s to coat the surface of basalt samples uniformly using a Leica EM ACE600 sputtering coater. SEM images were obtained by field emission scanning electron microscopy (SEM, Zeiss, Gemini300) with a working voltage of 20 kV.

Thermo-gravimetric analyses (Mettler-Toledo, Switzerland) were performed using 20 mg of sample. The heating rate was 20 °C·min^{-1}, and the temperature range was 30–1000 °C. The analyses were done in an N_2 atmosphere with a flow rate of 100 mL·min^{-1}.

3 Results and analysis

3.1 H_2 generation analysis

3.1.1 At 25 °C

Figure 3 shows the production of H_2 via basalt-CO_2-water reaction over 7 days of reaction in a small-bottle experiment. To assess the experimental error, replicate analyses (n = 3) were conducted for each sample, and the relative standard deviation (RSD)

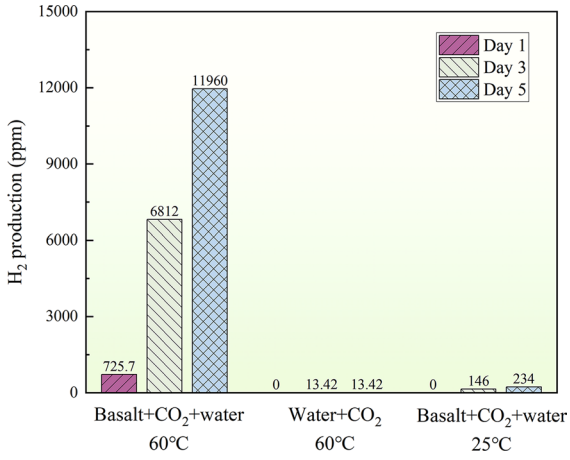


Fig. 4 H_2 production from water-CO_2-basalt rocks reactions at different temperatures

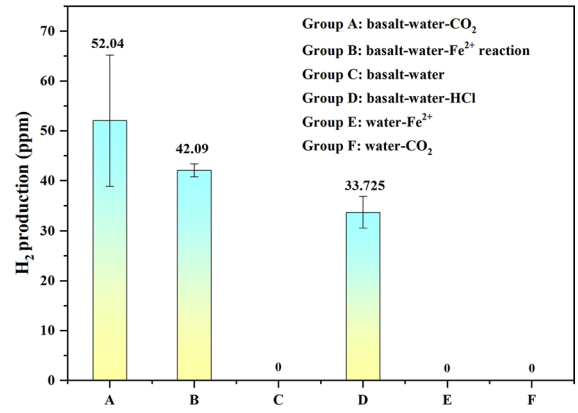


Fig. 5 H_2 generation with different influencing factors (1 day)

was calculated. The results show that basalt can produce H_2 in CO_2-saturated water at a mean rate of 46.68 ppm d^{-1}, with generation rates leveling off after 6 days. Noting that there is no CO_2 supply during the treatment to avoid H_2 leakage.

3.1.2 At 60 °C

CO_2 and water were injected into the basalt at the CarbFix site in Iceland at temperatures of 20–50 °C, and 95% of the CO_2 was mineralized in less than two years. To investigate the effect of temperature on the rate of H_2 production, we compared H_2 production at 60 °C with room temperature (about 25 °C). Figure 4 shows H_2 production from water-CO_2-basalt rocks reactions at different temperatures. At 60 °C, H_2 production increased steadily over 5 days, peaking at 11,960 ppm, with an average rate of 2,392 ppm per day, while at 25 °C, H_2 production only reached 234 ppm. The 5-day H_2 production at 60 °C was 51 times that at 25 °C. This indicates that elevated temperatures greatly enhanced H_2 production. Nevertheless, the results still strongly demonstrated the substantial enhancement of hydrogen production with increased temperature.

3.2 Effect of released Fe^{2+} on H_2 generation

Figure 5 shows the H_2 generation with different influencing factors. Results show that 52.04 ppm H_2 was produced in group A, while no H_2 was produced from group C, group E and group F. In group B (basalt-water-Fe^{2+}), similar amounts of H_2 (42.09 ppm) were produced with the addition of 2 mM Fe^{2+} to basalt suspensions, demonstrating the dissolved Fe^{2+} directly contributes to the H_2 production. In group C (basalt-water), no H_2 was produced within one day in the absence of CO_2, and no Fe^{2+} was released, indicating that Fe^{2+} released from the acid dissolution of basalt is crucial for H_2 production. In group D (basalt-water–HCl), 0.87 mM Fe^{2+} was released from the basalt, and ~33.7 ppm H_2 was produced. This H_2 production was lower than in the CO_2 system, likely due to the lower concentration of Fe(II) over time. The final pH values of the reaction solutions are shown in Table 3. The pH was 7.3 for the HCl-water system and 5.7 for the CO_2-saturated water system. This buffering effect of the CO_2 results in greater H_2 generation compared to the HCl-acidified system.

Table 3 The variation of Fe^{2+} concentration and pH before and after reaction

Group	Fe^{2+} concentration (mM)	pH before reaction	pH after reaction
A	2.3	5.0	5.7
B	2.3	6.3	6.5
C	0.24	10.9	10.7
D	0.87	5.0	7.3
E	2.3	6.6	6.6
F	0	3.3	3.3

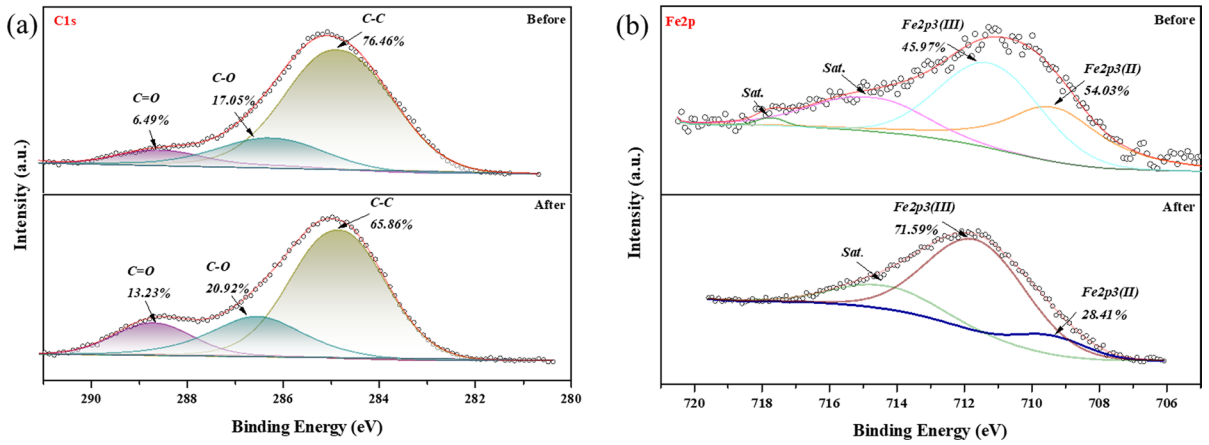


Fig. 6 **a** C 1s and **b** Fe2p XPS of basalt before and after reaction

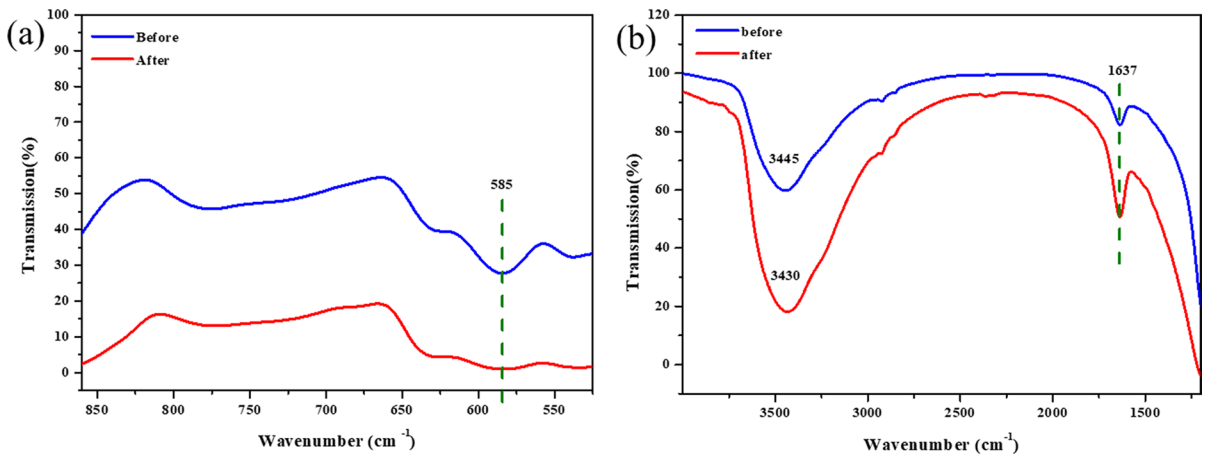


Fig. 7 FTIR spectra of basalt before and after reaction. **a** the Fe–O bond peak; **b** the hydroxyl peak

3.3 Analysis of Fe^{2+} and Fe^{3+} contents before and after reaction

The XPS results before and after reaction are shown in Fig. 6. High-resolution C 1s XPS revealed that the C=O content increased from 6.49% before the reaction to 13.23% after the reaction, which is likely due to the initial addition of CO_2 being ultimately fixed on the basalt surfaces as carbonates (Fig. 6a). The Fe2p spectra showed a decrease of Fe(II) from 54.03% prior to the reaction to 28.41% after the reaction, while Fe(III) increased from 45.97% to 71.59% (Fig. 6b). These results suggest that Fe(II) acts as an electron donor in the hydrogen production process from basalt, transferring electrons to H^+/H_2O, and reducing H^+ to hydrogen gas.

3.4 Analysis of basalt surface functional groups based on FTIR

FTIR results are shown in Fig. 7. The peak at 585 cm^{-1}, attributed to the Fe–O bond vibrational mode, weakened after the reaction, suggesting that Fe from the basalt was dissolved in ionic form during the reaction and was not re-deposited as Fe–O bonds (Fig. 7a). This reveals the release of Fe(II). Additionally, a blue shift in the hydroxyl peak from 3445 to 3430 cm^{-1} was observed after the reaction, indicating the breaking of hydrogen bonds of water molecules

Table 4 Changes in leachate ions before and after the reaction

Element	Before reaction (ppm)	After reaction (ppm)
Ca	188.0	3014.3
K	2298.6	1822.8
Mg	35.2	1701.5
Na	2749.7	2646.0
Al	104.4	9.3
Si	2329.0	2538.5
P	17.4	57.5
Ti	7.5	0
Mn	1.3	1.8
Fe	29.7	1.1

(Fig. 7b). During the reaction, water molecules dissociated on the basalt surface into hydroxyl groups and hydrogen ions. The hydrogen ions were reduced to hydrogen gas upon electron acquisition, enhancing the hydroxyl peak as the remaining hydroxyl groups were absorbed onto the basalt surface. This reveals the breakage of water molecules and denotes the origin of hydrogen ions which form H_2 in the reaction.

3.5 Changes in leachate ions before and after reaction based on ICP-MS

To reveal the variations in minerals throughout the processes, inductively coupled plasma mass spectrometry (ICP-MS) was conducted on the leachates before and after the basalt reaction. The results are shown in Table 4. The results indicate increased concentrations of Ca, Mg, and P in the post-reaction leachates, which can be attributed to the dissolution of Ca and Mg from the basalt into ionic form due to the acidity of carbonate acid. Conversely, the concentrations of Al, Ti, and Fe in the leachates decreased after the reaction, suggesting the formation of some secondary minerals. The results indicate increased concentrations of Ca, Mg, and P in the post-reaction leachates, which can be attributed to the dissolution of Ca and Mg from the basalt into ionic form due to the acidity of carbonate acid. Specifically, the dissolution of plagioclase feldspars and amphiboles, which are major components of basalt, releases significant amounts of Ca^{2+} and Mg^{2+} ions into the solution. Plagioclase feldspars, primarily composed of calcium and sodium aluminosilicates, are particularly susceptible to acid dissolution, leading to the release of Ca^{2+} ions. Similarly, amphiboles, which contain magnesium and iron, also contribute to the increase in Mg^{2+} ions. Conversely, the concentrations of Al, Ti, and Fe in the leachates decreased after the reaction, suggesting the formation of some secondary minerals. The decrease in Al^{3+} and Ti^{4+} concentrations can be attributed to the precipitation of aluminosilicate and titanium-based minerals. For instance, the formation of gibbsite ($Al(OH)_3$) and anatase (TiO_2) is likely to occur under these conditions, as these minerals are common secondary products in basaltic environments. The reduction in Fe^{2+} and Fe^{3+} concentrations indicate the precipitation of iron-rich minerals. The presence of both Fe^{2+} and Fe^{3+} suggests the formation of iron oxides and hydroxides, such as goethite (FeO(OH)) and hematite (Fe_2O_3). Additionally, the formation of siderite ($FeCO_3$) may also contribute to the decrease in Fe^{2+} concentration, as this mineral is known to precipitate in carbonate-rich environments.

3.6 Carbon mineralization observed by SEM, EMPA, and TG analysis

Significant differences in the surface morphology before and after treatments have been observed through SEM. As shown in Fig. 8a, the basalt surface before the reaction was smooth and flat. Substantial nano-sized mineral precipitates formed on the basalt surface, indicating mineral precipitation in the reaction process (Fig. 8b). To further determine the composition of the basalt's surface, EMPA was conducted. The EMPA results indicate that under ambient temperature conditions, carbonate minerals are formed after the reaction of basalt with CO_2 and water (Fig. 8c).

The mass of CO_2 fixed by basalt mineralization corresponds to the weight loss within the temperature range of 600–850 °C. Derivative thermogravimetric analysis (DTG) data shows that there is a significant weight loss in the post-reaction sample at 677.33 °C compared with the before-reaction sample, confirming the CO_2 mineralization after the basalt-CO_2-water reaction (Fig. 9). The mineral carbonation efficiency φ_{CO_2} was calculated to be 4.17% based on the following equations:

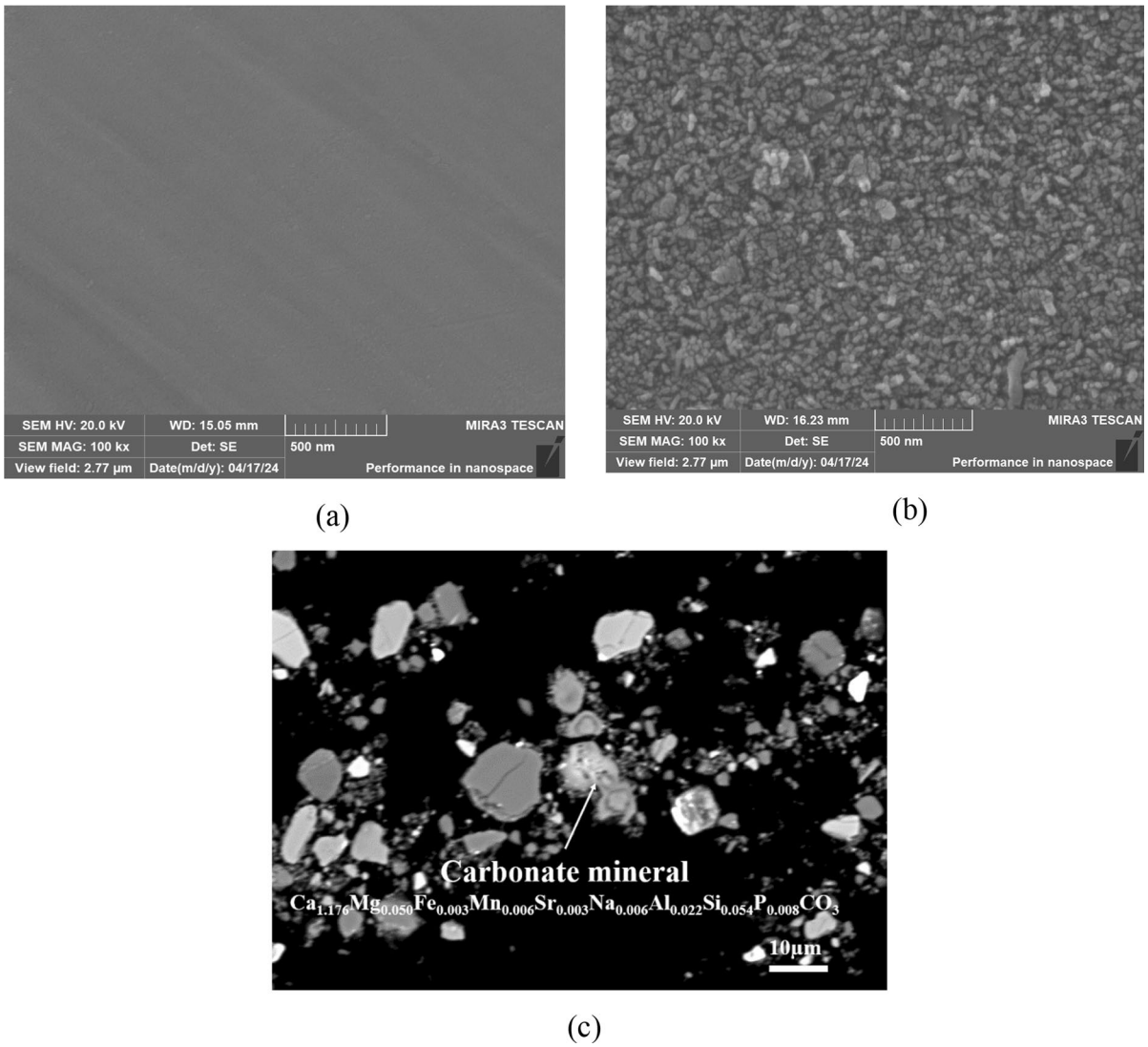


Fig. 8 SEM images of the basalt sample **a** before and **b** after water-CO_2-basalt reaction; **c** BSE images of formed carbonate minerals after water-CO_2-basalt reaction

$$\varphi_{CO_2}(\%) = \frac{m_{CO_2}}{m_0} \times 100\% = \frac{W_{ar,CO_2}(\%) - W_{br,CO_2}(\%)}{1 - [W_{ar,CO_2}(\%) - W_{br,CO_2}(\%)]} \times 100\% \quad (1)$$

$$W_{ar,CO_2}(\%) = W_{a1} - W_{a2} \quad (2)$$

$$W_{br,CO_2}(\%) = W_{b1} - W_{b2} \quad (3)$$

where $\varphi_{CO_2}(\%)$ is mineral carbonation efficiency, m_0 is the mass of basalt sample, m_{CO_2} is the mass of CO_2 fixed by the mineralization reaction, W_{a1} and W_{a2} are weight loss percentages corresponding to T_1 and T_2 on the TG curve of the sample before the reaction, respectively; W_{b1} and W_{b2} are weight loss percentages corresponding to T_1 and T_2 on the TG curve of the sample after the reaction, respectively; T_1 and T_2 are the temperatures of the two inflection points corresponding to the carbonate thermal decomposition peaks on the DTG curve of the sample after the reaction, $W_{ar,CO_2}(\%)$ and $W_{br,CO_2}(\%)$ are the weight loss percentages caused by the thermal decomposition

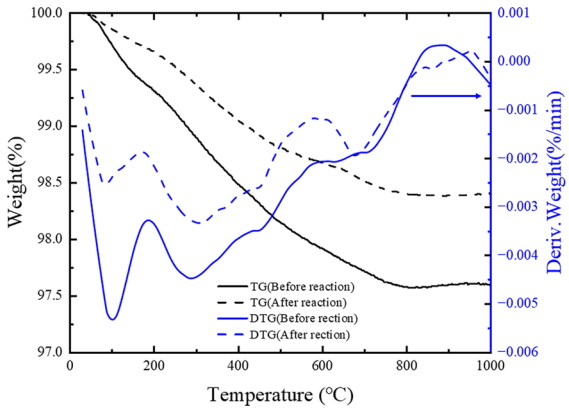


Fig. 9 TG and DTG analysis of the basalt sample before and after the basalt-CO_2-water reaction

of carbonates releasing CO_2, as determined by TG before and after the reaction, respectively.

The calculated CO_2 mineralization capacity for the studied three-month basalt-CO_2-water reaction is 41.7 kg CO_2 per ton. This observation is in line with previous studies that demonstrate that the metals contained in basalts are readily available to react with injected CO_2 to form carbonate minerals (Gislason and Oelkers 2014). Also, CO_2-charged water accelerates metal release from basalt (Table 4), favoring the formation of solid carbonate minerals. As a result, simultaneous H_2 generation and CO_2 sequestration were successfully obtained via the basalt-CO_2-water reaction.

4 Discussion

4.1 Reaction stoichiometry to generate H_2

In this paper, we report the potential of generating H_2 during CO_2 sequestration in basalt formations. The experimental results confirmed H_2 production and carbon mineralization, with a significant increase in H_2 production at 60 °C. Through a series of analyses, we revealed the important role of ferrous ion in hydrogen production. That is to say, ferrous-bearing minerals in basalt are essential for hydrogen production, such as pyroxene and olivine. These minerals release ferrous ions in a CO_2–HCO_3^--rich environment, which then exchange electrons with hydrogen ions from water ionization on the basalt surface. In this process, Fe^{2+} is oxidized to Fe^{3+}, while hydrogen ions are reduced to form hydrogen gas. The chemical reaction is as follows:

$$2Fe^{2+} - \text{basalt surface} + 2H^+ \rightarrow 2Fe^{3+} + H_2 \uparrow \quad (4)$$

This is similar to the well-known Schikorr reaction ($3Fe(OH)_2 \rightarrow Fe_3O_4 + 2H_2O + H_2\uparrow$) (Schikorr 1933). Previous studies reported the electron transfer between Fe^{2+} and water adsorbed to the rock surfaces promotes hydrogen generation (Mayhew et al. 2013).

4.2 Mechanism of generating H_2 during the CO_2 sequestration in basalt

The generation of H_2 during the basalt-CO_2-water reaction is fundamentally driven by the dissolution of ferrous-bearing minerals, particularly pyroxene and olivine, in the basalt matrix. These minerals release Fe^{2+} ions into solution under acidic conditions induced by CO_2-saturated water, as demonstrated by the ICP-MS analysis (Table 4). The subsequent electron transfer reactions involve Fe^{2+} ions acting as electron donors, which reduce protons (H^+) from water ionization to produce H_2 gas. Our experimental results confirmed several key mechanisms in the process:

(1) Acid-driven dissolution of basalt: CO_2 dissolution in water lowers the pH, facilitating the release of Fe^{2+} ions from the basalt structure. This process was corroborated by the FTIR data, which showed the weakening of Fe–O bonds, and the ICP-MS results that recorded significant increases in dissolved Fe concentration post-reaction.
(2) Electron transfer and H_2 generation: As observed in the XPS analysis, a decrease in Fe^{2+} content from 54.03 to 28.41% and a corresponding increase in Fe^{3+} content indicate that Fe^{3+} is oxidized during the reaction. This redox process simultaneously reduces H^+ ions, yielding H_2 gas.
(3) Surface-assisted reactions: SEM imaging revealed nano-sized precipitates on the basalt surface post-reaction, indicating active sites for water dissociation and H_2 generation. Additionally, the blue shift in the hydroxyl peak in FTIR spectra signifies the breaking of hydrogen bonds

in water, with hydroxyl groups absorbed onto the basalt surface aiding H_2 formation. FTIR data elucidated the dissociation of water on basalt surfaces, a critical step in generating protons for H_2 formation.

(4) Synergistic effects of CO_2: The buffering effect of CO_2-saturated water, as evident from the pH stabilization around 5.7, maintains a conducive environment for sustained Fe^{2+} release and subsequent H_2 generation. In comparison, HCl-acidified systems demonstrated lower H_2 yields, highlighting the unique role of the carbonate system in this mechanism.

(5) Role of temperature: Experimental results showed that increasing the reaction temperature from 25 to 60 °C enhanced the reaction rate and H_2 production by over 50-fold. Elevated temperatures likely accelerate the kinetics of mineral dissolution and redox processes, as supported by thermodynamic principles.

4.3 Potential engineering applications

Our experimental results show that the proposed concept has substantial potential for large scale application. However, transitioning from concept to reality requires addressing several challenges. Key issues include identifying the types of minerals and rocks capable of producing hydrogen, determining their hydrogen production efficiency, and understanding the behavior of hydrogen migration and accumulation in geological structures. The most critical concern is containing hydrogen underground to prevent surface escape. Insights can be drawn from natural hydrogen reservoirs to address this issue. The existence of natural hydrogen reservoirs and the development of hydrogen wells provide three key insights: (1) geological hydrogen production is feasible, as supported by our experimental results; (2) hydrogen can potentially be stored in geological structures. Documented natural hydrogen fluid barriers include dense shale (Pyrenees in Spain) and doleritic sills (Bourakébougou in Mali) (Prinzhofer et al. 2018; Hand 2023). It is hypothesized that low-porosity rock salt, granite, marble, or other thick, low-permeability rock layers could serve as natural hydrogen cap rocks; (3) extracting hydrogen from underground for commercial use is feasible. Mali's natural hydrogen well has been stably producing for 10 years, and the United States developed its first hydrogen well in 2019 (Hand 2023). In Australia, two drill holes specifically exploring natural hydrogen were very recently drilled (Gold Hydrogen, 2024).

Despite many challenges, the proposed technology for mineralized CO_2 storage and hydrogen production in basalt formations holds great promise. First, it proposed a new pathway for clean hydrogen, utilizing the giant, neglected hydrogen factory, i.e., within the Earth. Secondly, it brings additional revenue for CCS projects and ease the cost pressure. CO_2 that has been quickly mineralized in basalt formations can earn revenue through carbon trading markets, while the harvested hydrogen can be trading directly for profit. Thus, more attention should be focused on the promising method.

5 Conclusions

This work shows the potential of generating H_2 and geological storing CO_2 simultaneously in basalt reservoirs. The following conclusions can be drawn:

(1) H_2 is generated from basalt-CO_2-water reaction at a temperature of 25 °C, requiring neither extra energy input nor catalysts.

(2) The 5-day H_2 production at 60 °C was 51 times greater than that at 25 °C, suggesting the substantial enhancement of hydrogen production with increased temperature.

(3) Fe^{2+} plays a critical role in hydrogen production. CO_2 induces the acidic dissolution of basalt with Fe^{2+} release into solution, which promotes H_2 production during the CO_2 mineralization for sequestration.

(4) Carbon mineralization was observed by SEM, EMPA and TG analysis, with the mineral carbonation efficiency of 4.17% in 3 months.

Acknowledgements We thank Dr. Longxia Wu from the Core Facility of Wuhan University for her assistance with XPS analysis.

Author contributions L. Huang, Y. Liu, and X. Tang: Writing-original draft, Writing-review & editing, Data curation. Q. Liu: Conceptualization, Methodology, Supervision. Y. Zhang: Data Curation, Visualization. C. Steefel, M. Hu, and S. Liu: Methodology and Supervision. All authors reviewed the manuscript.

Funding This work was financially supported by the Fundamental Research Funds for the Central Universities (Grant No. 2042024rs0001), the Key Laboratory of Safety for Geotechnical and Structural Engineering of Hubei Province, and National Natural Science Foundation of China (Grant No. 52270165 and 42402285), and the Postdoctoral Fellowship Program (Grade B) of China Postdoctoral Science Foundation (Grant No. GZB20230544).

Data availability The data that support the findings of this study are available in Zenodo at http://doi.org/https://doi.org/10.5281/zenodo.13329052, including experimental data of XPS, FTIR, EMPA, H_2 production, ICP-MS, Fe^{2+} concentration, and pH testing results.

Declarations

Competing Interests The authors declare no competing interests.

Open Access This article is licensed under a Creative Commons Attribution-NonCommercial-NoDerivatives 4.0 International License, which permits any non-commercial use, sharing, distribution and reproduction in any medium or format, as long as you give appropriate credit to the original author(s) and the source, provide a link to the Creative Commons licence, and indicate if you modified the licensed material. You do not have permission under this licence to share adapted material derived from this article or parts of it. The images or other third party material in this article are included in the article's Creative Commons licence, unless indicated otherwise in a credit line to the material. If material is not included in the article's Creative Commons licence and your intended use is not permitted by statutory regulation or exceeds the permitted use, you will need to obtain permission directly from the copyright holder. To view a copy of this licence, visit http://creativecommons.org/licenses/by-nc-nd/4.0/.

References

Aradóttir ESP, Sonnenthal EL, Björnsson G, Jónsson H (2012) Multidimensional reactive transport modeling of CO_2 mineral sequestration in basalts at the Hellisheidi geothermal field, Iceland. Int J Greenh Gas Control 9:24–40

Blay-Roger R, Bach W, Bobadilla LF et al (2024) Natural hydrogen in the energy transition: fundamentals, promise, and enigmas. Renew Sustain Energy Rev. https://doi.org/10.1016/j.rser.2023.113888

Boreham CJ, Edwards DS, Czado K et al (2021) Hydrogen in Australian natural gas: occurrences, sources and resources. APPEA J 61:163–191

Bui M, Adjiman CS, Bardow A et al (2018) Carbon capture and storage (CCS): The way forward. Energy Environ Sci 11:1062–1176. https://doi.org/10.1039/c7ee02342a

Durmaz T (2018) The economics of CCS: Why have CCS technologies not had an international breakthrough? Renew Sustain Energy Rev 95:328–340. https://doi.org/10.1016/j.rser.2018.07.007

Evro S, Oni BA, Tomomewo OS (2024) Carbon neutrality and hydrogen energy systems. Int J Hydrogen Energy 78:1449–1467. https://doi.org/10.1016/j.ijhydene.2024.06.407

Fender TD, Van Der Land C, Rouainia M et al (2020) The assessment of organic matter young's modulus distribution with depositional environment and maturity. J Geophys Res Solid Earth. https://doi.org/10.1029/2020JB020435

Gislason SR, Oelkers EH (2014) Carbon storage in basalt. Science 344:373–374

Greening C, Biswas A, Carere CR et al (2016) Genomic and metagenomic surveys of hydrogenase distribution indicate H2 is a widely utilised energy source for microbial growth and survival. ISME J 10:761–777

Hand E (2023) Hidden hydrogen: does earth hold vast stores of a renewable, carbon-free fuel? Science 336:630–636

Kainiemi L, Eloneva S, Toikka A et al (2015) Opportunities and obstacles for CO_2 mineralization: CO_2 mineralization specific frames in the interviews of Finnish carbon capture and storage (CCS) experts. J Clean Prod 94:352–358. https://doi.org/10.1016/j.jclepro.2015.02.016

Kelley DS, Karson JA, Fruh-Green GL et al (2005) A serpentinite-hosted ecosystem: the Lost city hydrothermal field. Science 307:1428–1434

Kularatne K, Sissmann O, Kohler E et al (2018) Simultaneous ex-situ CO_2 mineral sequestration and hydrogen production from olivine-bearing mine tailings. Appl Geochem 95:195–205. https://doi.org/10.1016/j.apgeochem.2018.05.020

Leong JAM, Shock EL (2020) Thermodynamic constraints on the geochemistry of low-temperature, continental, serpentinization-generated fluids. Am J Sci 320:185–235. https://doi.org/10.2475/03.2020.01

Longden T, Beck FJ, Jotzo F et al (2022) 'Clean' hydrogen? – Comparing the emissions and costs of fossil fuel versus renewable electricity based hydrogen. Appl Energy. https://doi.org/10.1016/j.apenergy.2021.118145

Mahjour SK, Faroughi SA (2023) Risks and uncertainties in carbon capture, transport, and storage projects: a comprehensive review. Gas Sci Eng 119:205117. https://doi.org/10.1016/j.jgsce.2023.205117

Matter JM, Stute M, Snæbjörnsdottir SÓ et al (2016) Rapid carbon mineralization for permanent disposal of anthropogenic carbon dioxide emissions. Science 352:1312–1314

Mayhew LE, Ellison ET, Mccollom TM et al (2013) Hydrogen generation from low-temperature water–rock reactions. Nat Geosci. https://doi.org/10.1038/ngeo1825

McCollom TM, Bach W (2009) Thermodynamic constraints on hydrogen generation during serpentinization of ultramafic rocks. Geochim Cosmochim Acta 73:856–875. https://doi.org/10.1016/j.gca.2008.10.032

McGrail BP, Schaef HT, Spane FA et al (2017) Field validation of supercritical CO_2 reactivity with basalts. Environ Sci Technol Lett 4:6–10. https://doi.org/10.1021/acs.estlett.6b00387

Milkov AV (2022) Molecular hydrogen in surface and subsurface natural gases: abundance, origins and ideas for deliberate exploration. Earth Sci Rev 230:104063

Momirlan M, Veziroglu TN (2002) Current status of hydrogen energy. Renew Sustain Energy Rev 6:141–179

Osselin F, Pichavant M, Champallier R et al (2022) Reactive transport experiments of coupled carbonation and serpentinization in a natural serpentinite. Implication for hydrogen production and carbon geological storage. Geochim Cosmochim Acta 318:165–189

Prinzhofer A, Tahara Cissé CS, Diallo AB (2018) Discovery of a large accumulation of natural hydrogen in Bourakebougou (Mali). Int J Hydrogen Energy 43:19315–19326. https://doi.org/10.1016/j.ijhydene.2018.08.193

Rutqvist J (2012) The geomechanics of CO_2 storage in deep sedimentary formations. Geotech Geol Eng 30:525–551

Schikorr G (1933) The iron (II) hydroxide and a ferromagnetic iron (III) hydroxide. Z Anorg Allg Chem 212:33–39

Smith NJP, Shepherd TJ, Styles MT, Williams GM (2005) Hydrogen exploration: a review of global hydrogen accumulations and implications for prospective areas in NW Europe. In: Geological society, London, petroleum geology conference series. pp 349–358

Sun L, Chen W (2022) Impact of carbon tax on CCUS source-sink matching: finding from the improved ChinaCCS DSS. J Clean Prod 333:130027. https://doi.org/10.1016/j.jclepro.2021.130027

Truche L, McCollom TM, Martinez I (2020) Hydrogen and abiotic hydrocarbons: molecules that change the world. Elem Int Mag Mineral Geochem Petrol 16:13–18

Yue M, Lambert H, Pahon E et al (2021) Hydrogen energy systems: a critical review of technologies, applications, trends and challenges. Renew Sustain Energy Rev 146:111180. https://doi.org/10.1016/j.rser.2021.111180

Zgonnik V (2020) The occurrence and geoscience of natural hydrogen: a comprehensive review. EaRth-Sci Rev 203:103140. https://doi.org/10.1016/j.earscirev.2020.103140

Publisher's Note Springer Nature remains neutral with regard to jurisdictional claims in published maps and institutional affiliations.